Support information

Heteroatom doping-induced formation of closed pores for high-performance sodium storage hard carbon anodes

Wenbo Hou,[‡a] Lili Ma,[‡a] Anbai Li,[a] Hui Peng,[a] Zhiyuan Liu,[a] Xin Wang,[a] Kanjun Sun,[b] Guofu Ma,*[a] Yuxi Xu*[c]

[a]Key Laboratory of Eco-Functional Polymer Materials of the Ministry of Education, Key Laboratory of Polymer Materials of Gansu Province, College of Chemistry and Chemical Engineering, Northwest Normal University, Lanzhou 730070, China.

[b]College of Chemistry and Chemical Engineering, Lanzhou City University, Lanzhou 730070, China.

[c]School of Engineering, Westlake University, Hangzhou 310024, China.

[‡]W. Hou and L. Ma contributed equally to this work.

E-mail: magf@nwnu.edu.cn (G. Ma), xuyuxi@westlake.edu.cn (Y. Xu)

S1 Experimental

S1.1 Materials

Resorcinol, thiourea, formaldehyde, N-methylpyrrolidone (NMP) and anhydrous ethanol were purchased from Aladdin Chemical Company. The chemicals were analytical grade reagents without further purification.

S1.2 Synthesis of precursor RTF resin

Briefly, 0.5 mL of ammonia, 40 mL of anhydrous ethanol and 100 mL of distilled water were mixed homogeneously at 70 °C, followed by the addition of 0.55 g of resorcinol and 0.75 mL of formaldehyde, and stirring for 30 min. Then, 0.75 g of thiourea and 0.55 mL of formaldehyde were added, and stirring was performed for 24 h. The mixture was then introduced into a 50 mL autoclave with Teflon-inner, and the reaction was held at 120 °C for 24 h. The obtained resorcinol-thiourea-formaldehyde (RTF) resin was collected by centrifugation and repeatedly washed with ethanol. Finally, the product of RTF resin was dried under vacuum oven at 60°C.

For comparison, RF resin was also prepared by the same reaction condition as RTF, but without the addition of no thiourea.

S1.3 Preparation of CDRTF and CDRF

The RTF resin was held at 350 °C for 2 h in a quartz furnace tube under flowing nitrogen atmosphere with a heating rate of 5 °C min^{-1}, and then continued to be heated to 1200 °C for 2 h. After being cooled to room temperature, the resulting carbon material was named as CDRTF. The same experimental steps were used to carbonize RF to obtain CDRF without N and S doping.

S2 Material characterization

The morphology of the products was examined by field emission scanning electron microscopy (FE-SEM, Ultra Plus, Carl Zeiss, Germany) at an accelerating voltage of 5.0 kV. The microstructure of the samples was characterized by transmission electron microscopy (TEM, Carl Zeiss, Germany). The

Brunner-Emmett-Taylor (BET) surface area (S_{BET}) of the samples was analyzed by nitrogen adsorption and desorption on a Micromeritics ASAP 2020 nitrogen adsorption instrument (USA). All samples were degassed at 300 °C prior to nitrogen adsorption measurements. X-ray diffraction (XRD) of the samples was performed on an advanced diffractometer (D/Max-2400, Rigaku) using Cu Kα radiation (k = 1.5418 Å), 40 kV, 100 mA. The 2θ range used in the measurements was to 80°. X-ray photoelectron spectroscopy (XPS) measurements were performed on a K-Alpha system (USA) using a monochromatic Al Kα radiation source. Raman spectroscopy was conducted by employing a Horiba Scientific LabRAM HR-Evolution.

S3 Electrochemical characterization

For the fabrication of CDRTF anode, 80 wt% of CDRTF active material, 10 wt% of Super P and 10 wt% of polyvinylidene fluoride (PVDF) were mixed in NMP, and then the mixed slurry was uniformly coated on a copper foil, which was dried in a vacuum drying oven at 80 °C overnight. Subsequently, the coated copper foil was cut into circular electrode sheets of 12 mm in diameter under the pressure of 10 M Pa. The mass of the active material of the electrode sheet was 0.8-1.0 mg.

The electrode sheets were assembled to half-cell in a CR2032 coin cell in a glove box filled with Ar atmosphere with a content of H_2O and O_2 lower than 0.1 ppm using a sodium foil with a diameter of 15 mm as the reference electrode and 1 M $NaPF_6$ in DIGLYME (100 Vol%) as electrolyte.

To make the full cell, the CDRTF anode was first charged and discharged several times at a current density of 0.05 A g^{-1} with a cutoff voltage of 0.2 V. The pre-sodiumized CDRTF anode was then stripped in a glove box. Then, the CDRTF anode and AC cathode were assembled in a CR2032 coin cell using glass fiber (Whatman, GF/D) and 1 M $NaPF_6$ in EC : PC=1:1 Vol% with 5% FEC as separator and electrolyte, respectively.

Galvanostatic charge/discharge (GCD) measurement was performed on the Neware battery test system with a voltage range of 0.01-3 V (vs Na^+/Na) at room temperature. An electrochemical

workstation (CHI 660E, Chenhua, Shanghai) was used for CV and EIS measurements.

GITT is considered to be an effective method for evaluating the apparent diffusion coefficient of ions at different equilibrium potentials. The Na^+ diffusion coefficient (D_K) can be calculated according to Fick's second law with the equation:

$$D_k^+ = \frac{4}{\pi\tau}\left(\frac{m_B V_M}{M_B S}\right)^2 \left(\frac{\Delta E_S}{\Delta E_\tau}\right)^2$$

where τ is the relaxation time of the electrode, m_B, M_B, V_M and S denote the mass of electrode active material, molar volume, molar mass, and electrode area of the electrode active substance, respectively. ΔE_s and ΔE_τ represent voltage changes caused by the galvanostatic current discharge and pulse, respectively.
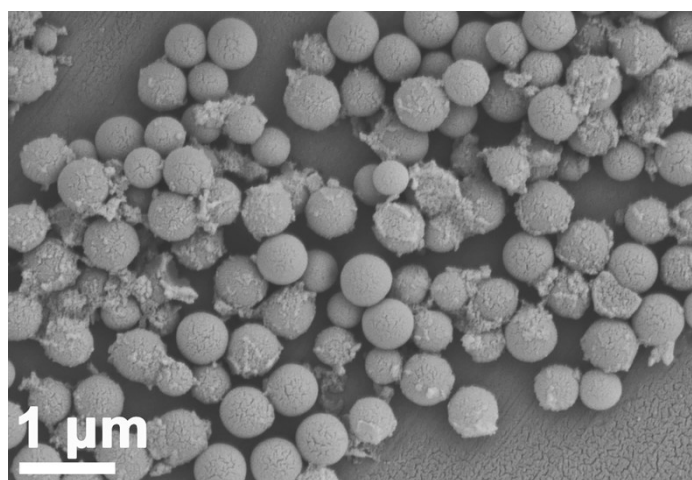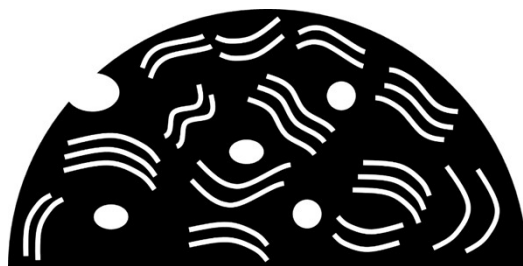
Fig. S1 SEM image of RTF.
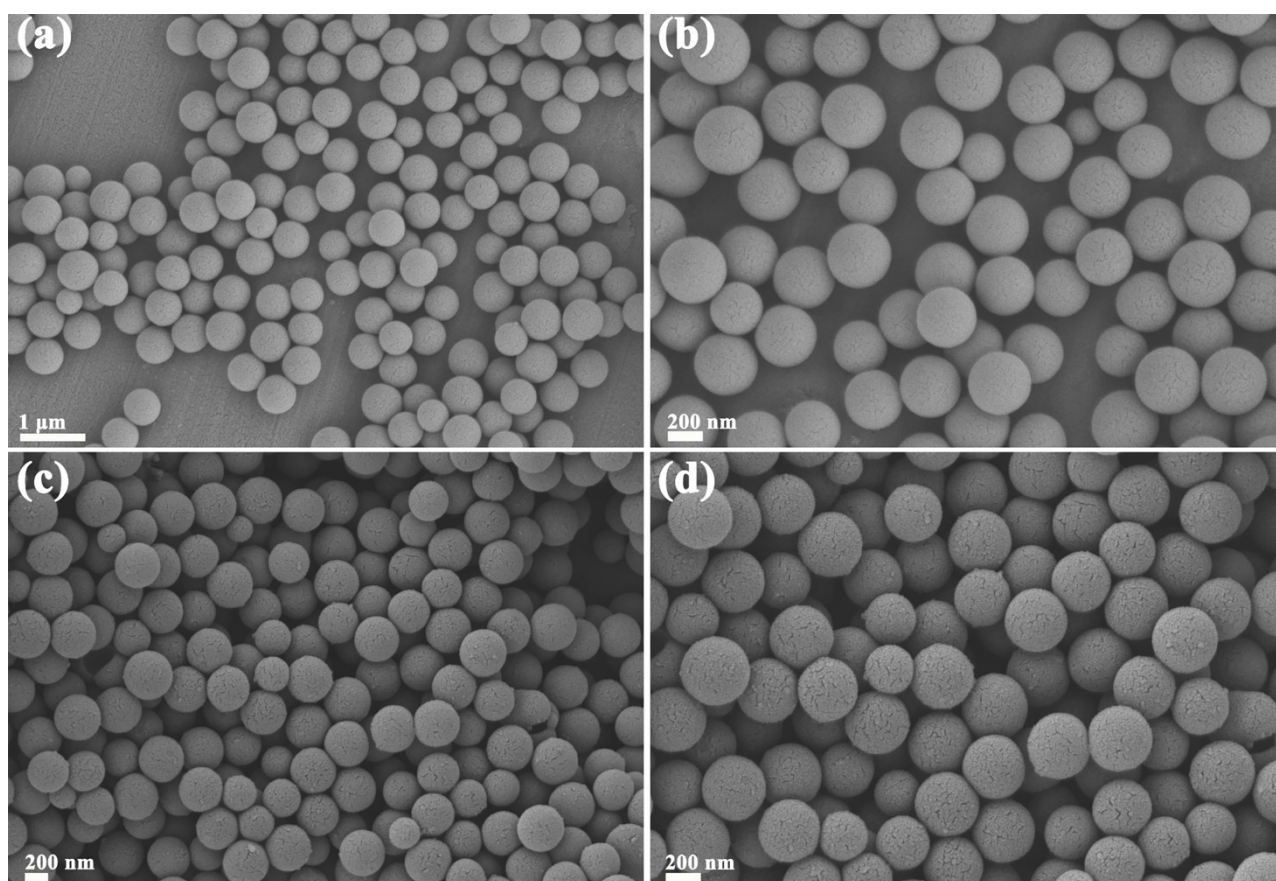
Fig.S2 SEM images of (a-b) RF and (c-d) CDRF.
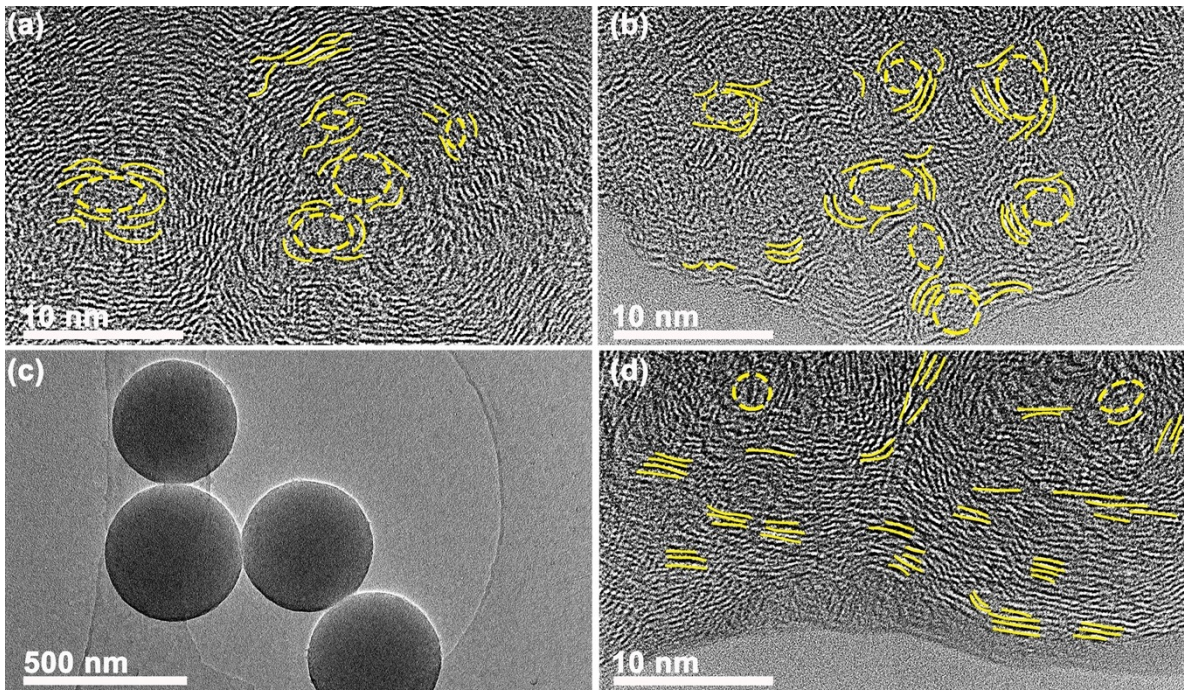
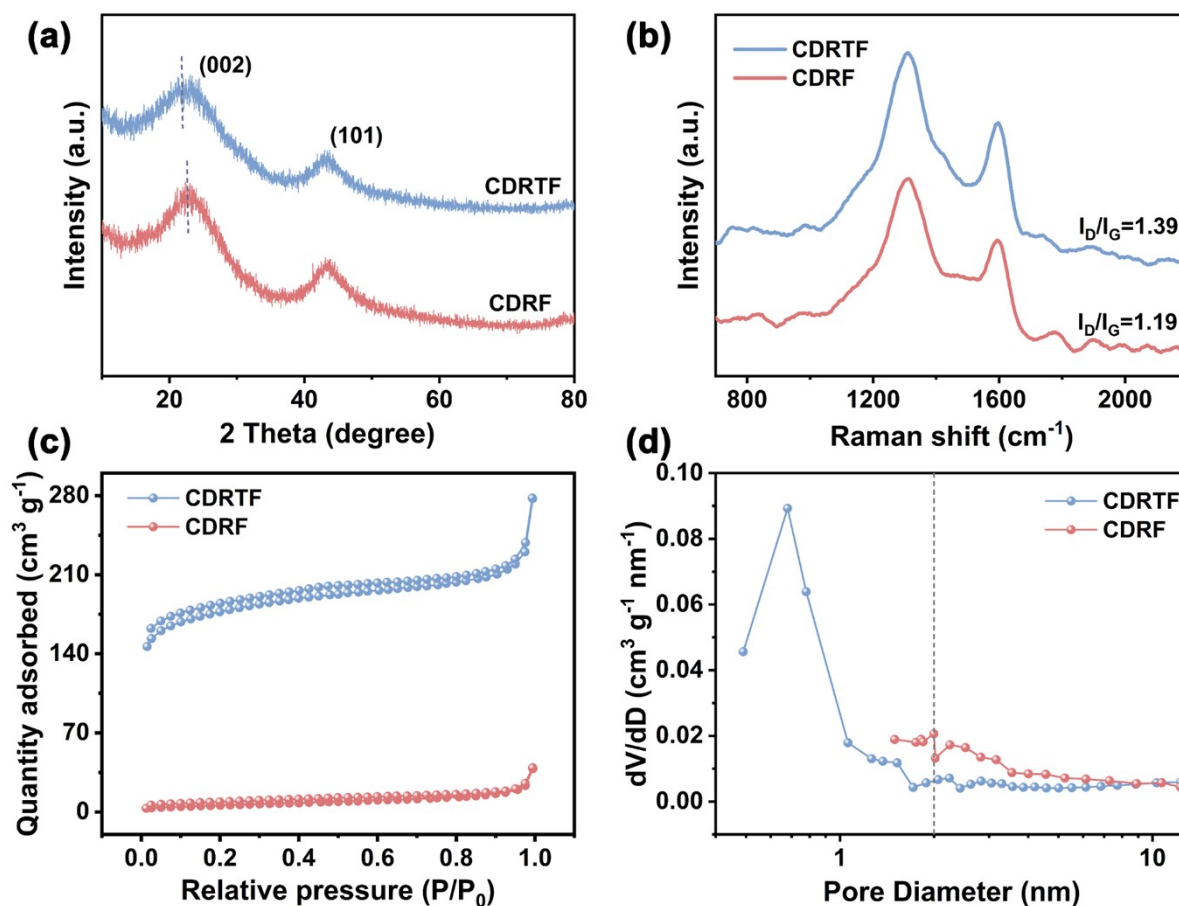**Fig. S3** (a-b) HRTEM images of CDRTF, (c)TEM and (d) HRTEM images of CDRF.

Fig. S4 Schematic diagram of pore structure evolution during heat treatment process.

Fig. S5 (a) XRD patterns, (b) Raman spectra, (c) N_2 adsorption/desorption isotherms, (d) pore size distribution of CDRTF and CDRF.

The X-ray diffraction (XRD) patterns of CDRTF and CDRF are shown in Fig. S6a. The XRD patterns of all the samples show two peaks near ~22.3° and ~42.6°, which correspond to the (002) and (101) planes of the carbon material, respectively. In contrast to the XRD patterns of the CDRF material, the (002) peak of the CDRTF appears to be shifted towards a lower diffraction angle, indicating that the interval spacing of the CDRTF increases, which is consistent with the TEM test results. The increase in lattice spacing in the CDRTF can be originated from the doping of S and N, which causes the distortion of the six-membered cyclic carbon skeleton[1]. The large layer spacing in CDRTF is more favorable for the transport of Na^+.

Fig. S5b shows that Raman spectra of the CDRF and CDRTF, where two broad peaks at about 1310 cm^{-1} and 1595 cm^{-1} are attributed to the disordered bands (D bands) and graphite bands (G bands)

of the carbon material[2]. In general, the D bands denote defects in the carbon lattice, while the G bands denote the tensile vibrations in the sp^2 hybridization plane of the carbon. In comparison to the low peak intensity ratio (I_D/I_G) value of the CDRF, the CDRTF reflects a higher value of I_D/I_G of 1.39, which is attributed to the large number of defects introduced by the heteroatoms doping. Highly defects in carbon materials can provided abundant Na^+ reactive sites and improves Na^+ storage capacity. The specific surface area and the porosity degree of the carbon materials were further investigated using nitrogen adsorption/desorption isotherm tests, as shown in Fig. S5c. The adsorption isotherms of the two materials exhibited type I characteristic with type H4 hysteresis, which is consistent with the expected adsorption behaviors of the micro/mesoporous materials. In addition, CDRTF appeared a continuous adsorption capacity at relatively high pressures, showing the material in the relatively large crack porous structure. The hierarchical porous structure in CDRTF is conducive to the diffusion of Na^+ and promote the electrolyte diffusion and promotes electrolyte penetration. According to the Brunauer-Emmett -Teller (BET) method, the specific surface areas (S_{BET}) of the CDRTF and CDRF anodes were calculated to be 137.3 m^2 g^{-1} and 21.8 m^2 g^{-1}, respectively. The pore size distributions of the CDRTF and CDRF materials as shown in Fig. S5 d. One can see that the CDRTF is mainly dominated by a large number of micropores and a small amount of mesopores, which originates from the evaporation of heteroatoms and in-situ reconstruction of cavities to form closed pores during the high temperature carbonization process. This closed pore structure is important for the storage of Na^+.
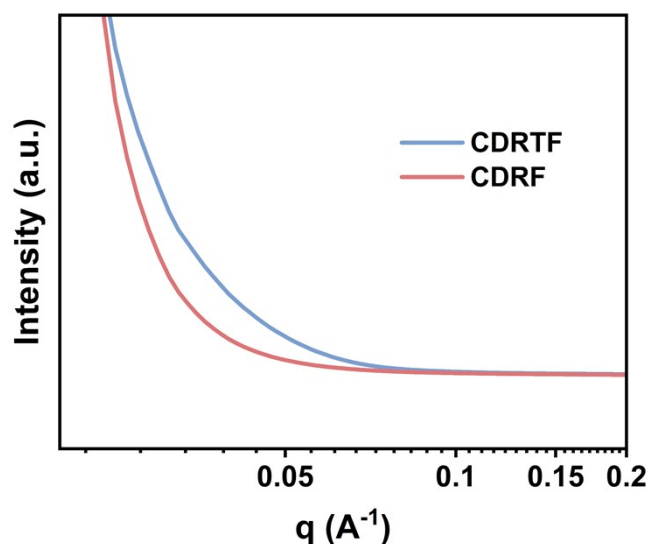
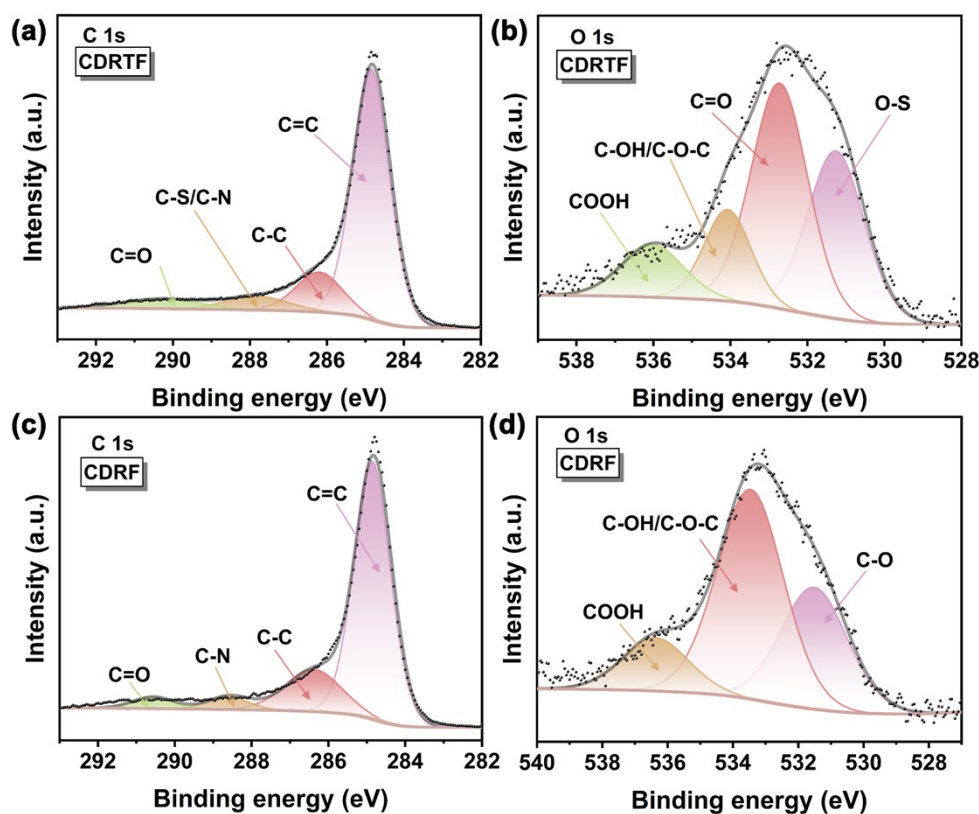**Fig. S6** Small-angle X-ray scattering patterns.

Fig. S7 (a) C 1sand (b) O 1s XPS spectra of CDRTF, (c) C 1s and (d) O 1s XPS spectra of CDRF.

The C 1s pattern of the CDRTF anode is shown in Fig. S7 (a), which contains four carbon components as C=C (284.9 eV), C-C (286.2 eV), C-S/C-N (287.8 eV), and C=O (290.3 eV)[3], in which the appearance of C-S and C-N indicates the successful doping of N and S. The O 1s pattern is shown in Fig. S7b, was fitted to four peaks as O-S (531.25 eV), C=O (532.75 eV), C-OH/C-O-C (534.1 eV),

and COOH (536.15 eV)[4], in which the presence of C=O and COOH facilitates the infiltration of the electrolyte in the anode of the CDRTF, which contributes to the storage of Na+.

The C 1s spectrum of the contrast sample CDRF anode is shown in Fig. S7c, which contains C=C (284.85 eV), C-C (286.45 eV), C-N (288.64 eV), and C=O (290.6 eV)[3], with a small amount of C-N originating from resorcinol in the raw material, and the O 1s spectrum of the CDRF, as shown in Fig. S7d. which contains C-O (531.55 eV), C-OH/C-O-C (533.45 eV) and COOH (536.4 eV)[4].
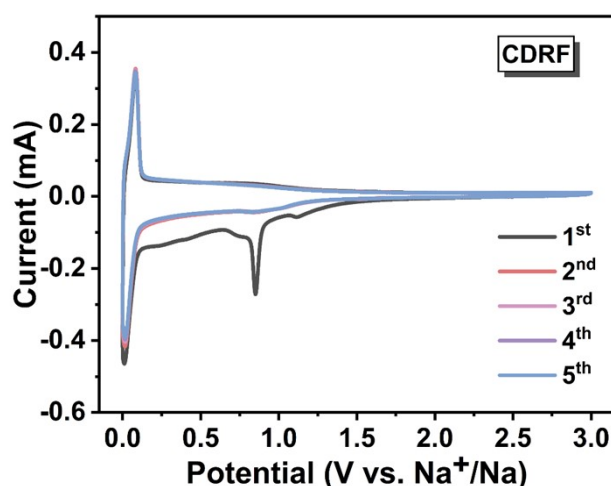
Fig. S8 CV plots of CDRF anode at 0.1 mV s^{-1}.

During the first-lap discharge process, compared with the CDRTF anode, the reduction peak formed by the CDRF anode due to electrolyte decomposition is more obvious, indicating that the CDRF anode is not as well infiltrated with the electrolyte as the CDRTF, thus prompting a large amount of electrolyte decomposition to form the SEI film.
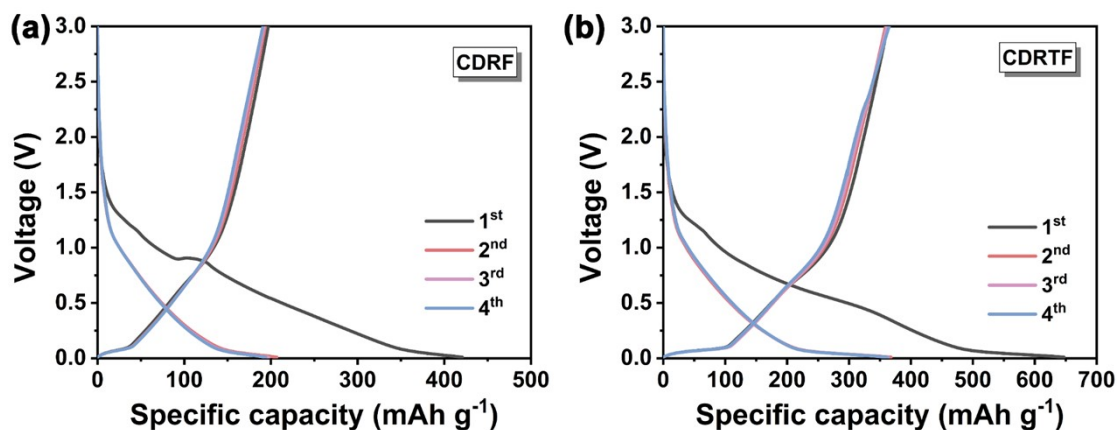
Fig. S9 GCD plots of (a) CDRF and (b) CDRTF at 0.05 A g^{-1}.

As shown in Fig. S9, the first discharge and charge capacities of the CDRF anode and CDRTF anode at 0.05 A g^{-1} were 420.86 mAh g^{-1}, 196.99 mAh g^{-1} and 647.53 mAh g^{-1}, 362.69 mAh g^{-1}, with initial Coulombic efficiencies (ICE) of about 46 % and 56 %, respectively. A slightly high ICE for the CDRTF anode is originated from the heteroatoms doping, which induced a larger layer spacing of the carbon material and more microporous structures, accelerating the infiltration of the electrolyte and the transport of ions.
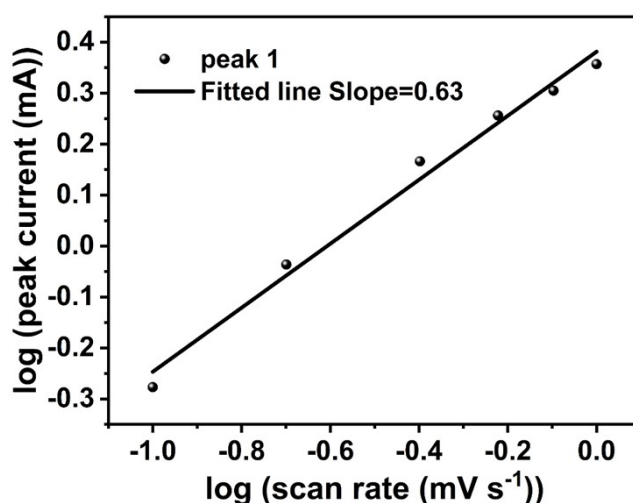
Fig. S10 *b* value of peak current.

In general, the *b* value is used to respond to the diffusion process induced by Na$^+$ intercalation/excavation (*b*=0.5) and the capacitive behavior of the bilayer induced by the surface Faraday redox reaction (*b*=1). The *b* value can be calculated by the equation: $i=av^b$, where *i* denotes the peak current, *v* denotes the scanning rate, and *b* value is used to respond to the diffusion process induced by the Na$^+$ intercalation/excavation. As shown, the *b* value of CDRTF is calculated to be 0.63 within 0.1-1.0 mV s^{-1}, respectively, indicating that the two sodium storage modes act synergistically and are dominated by the intercalation type.
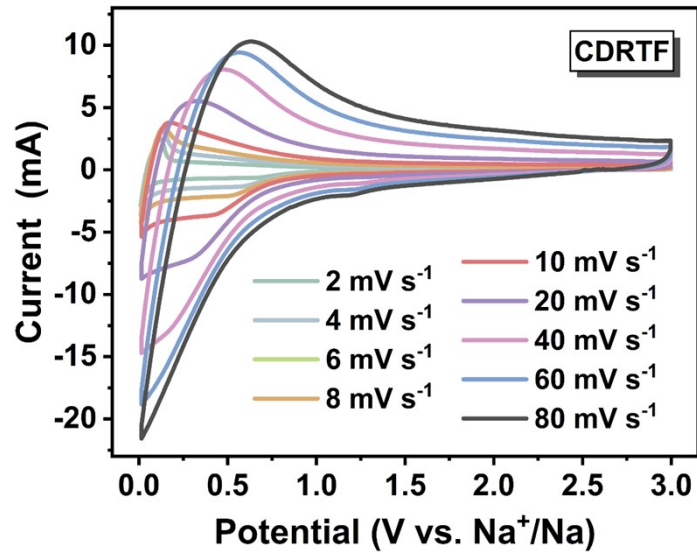
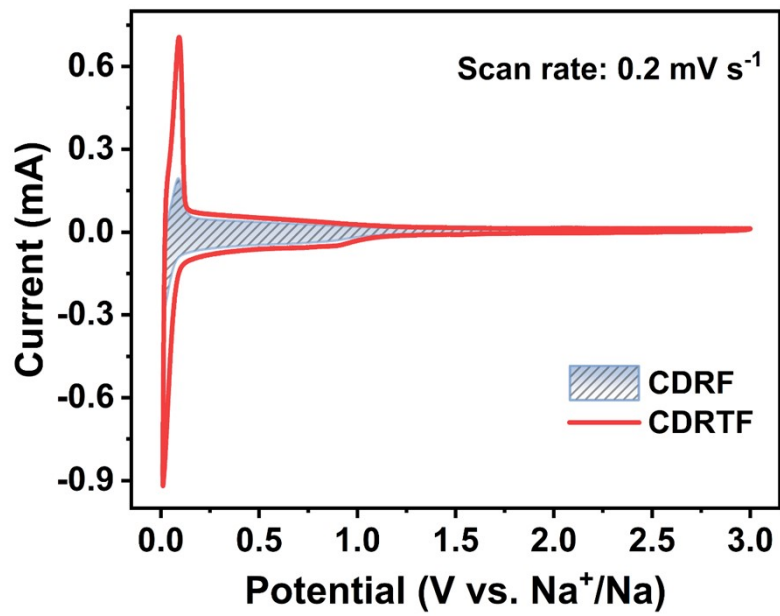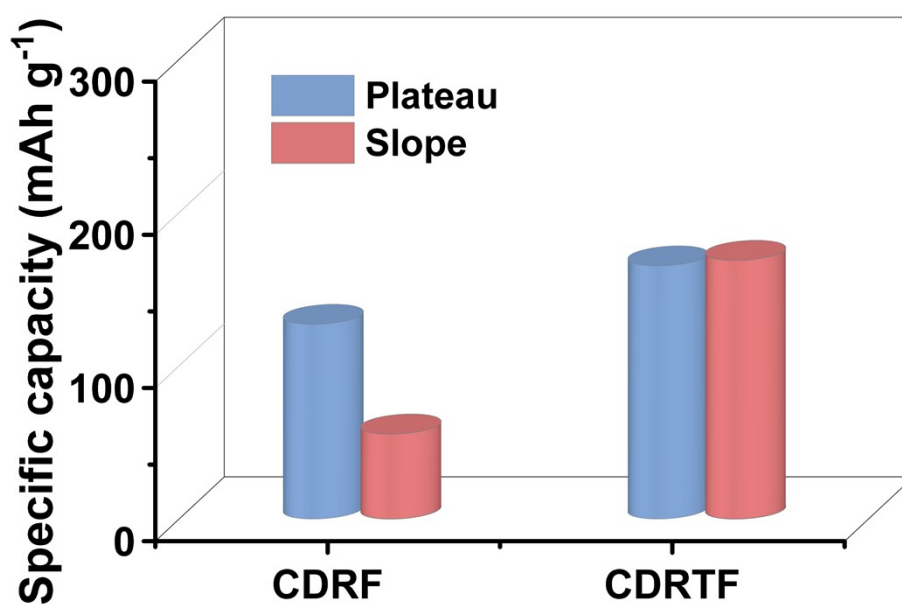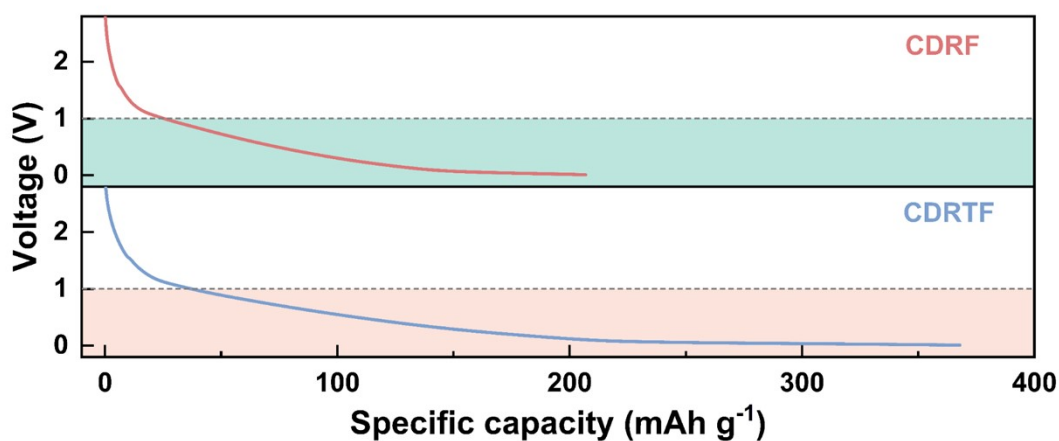**Fig. S11** CV curves of CDRTF at 2-80 mV s^{-1}.

Fig. S12 CV area comparison at the same sweep speed.

Fig. S13 Comparison of the plateau and sloping capacity of CDRTF and CDRF based on the 2nd discharge/charge curves.

Fig. S14 Comparison of capacity below 1.0 V at 0.05 A g^{-1}.

In the "insertion-filling zone" below 1.0 V, the discharge specific capacity of CDRTF anode is much higher than that of CDRF anode, which is attributed to the wider layer spacing and more closed-pore structure of CDRTF. The increased layer spacing accelerates the shuttling of Na$^+$ as well as the introduction of closed-pore structure by heteroatom doping, which is more conducive to the filling of Na$^+$, thus increasing the capacity of the "intercalation-filling zone".
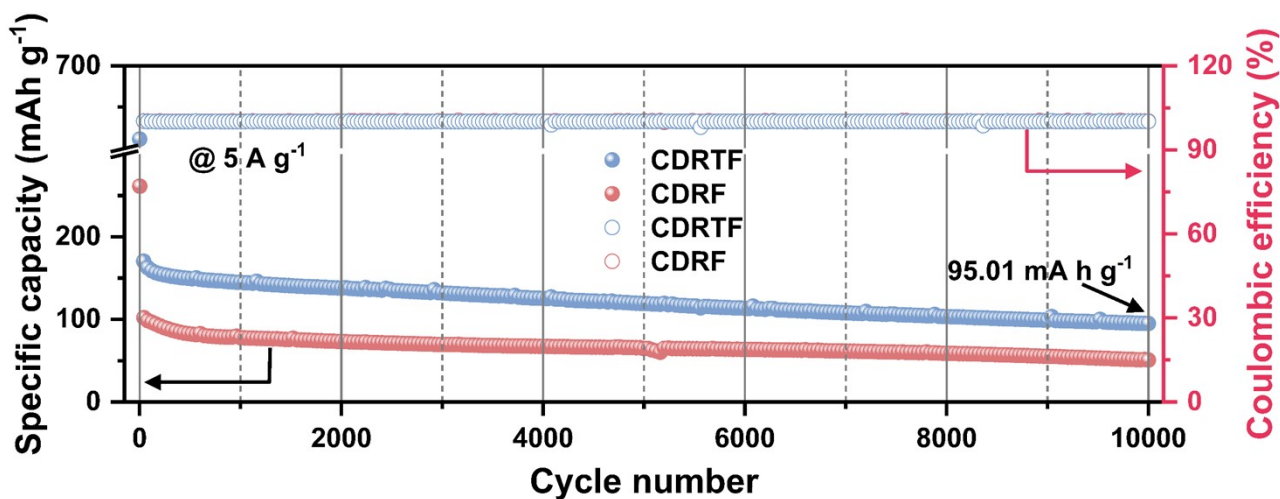
Fig. S15 Long cycling performance of CDRF and CDRTF at 5 A g^{-1}.
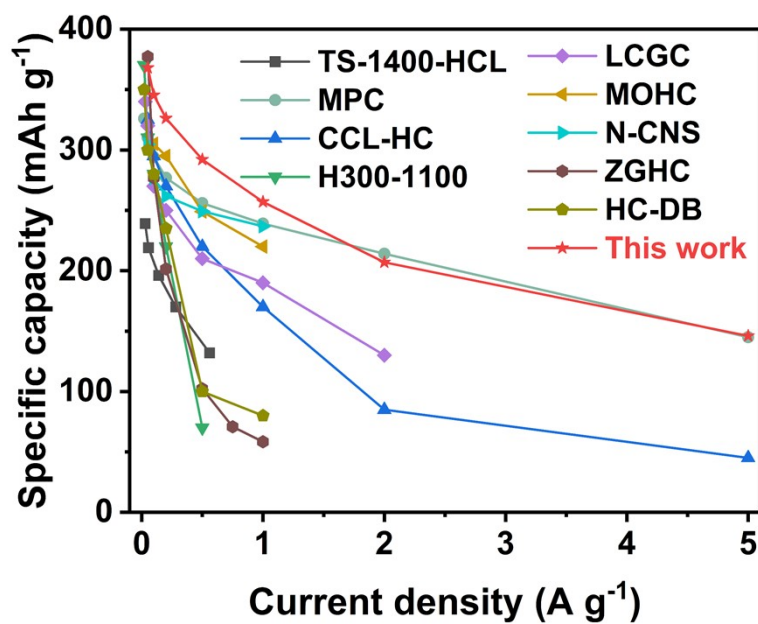

Fig. S16 Comparison of this study with other hard carbon capacities reported in the literature.[5-14]
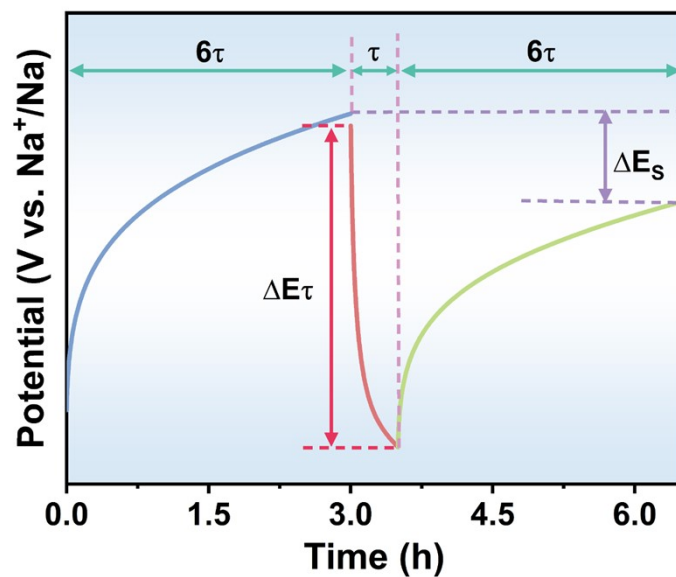
Fig. S17 Schematic representation of basic parameters analyzed by GITT during the initial charge/discharge process.
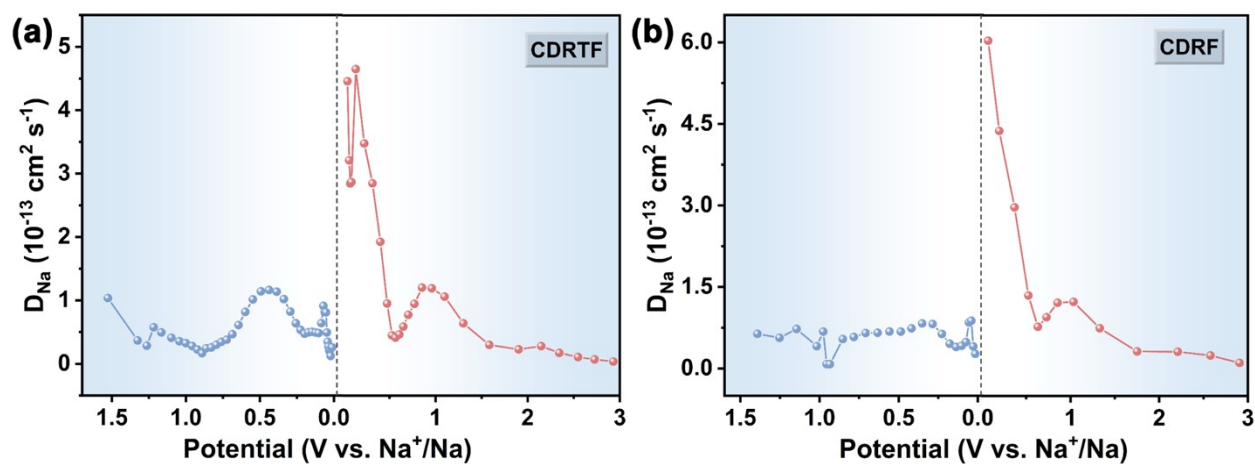

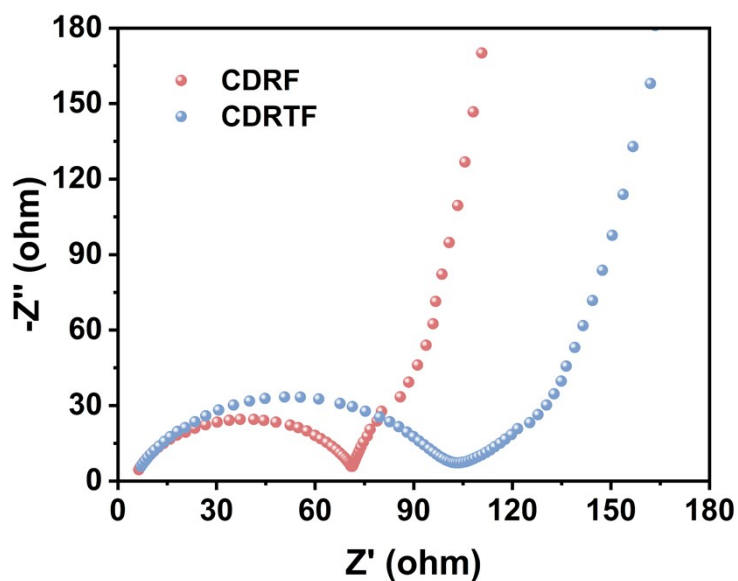**Fig. S18** Diffusion rates for CDRTF and CDRF.

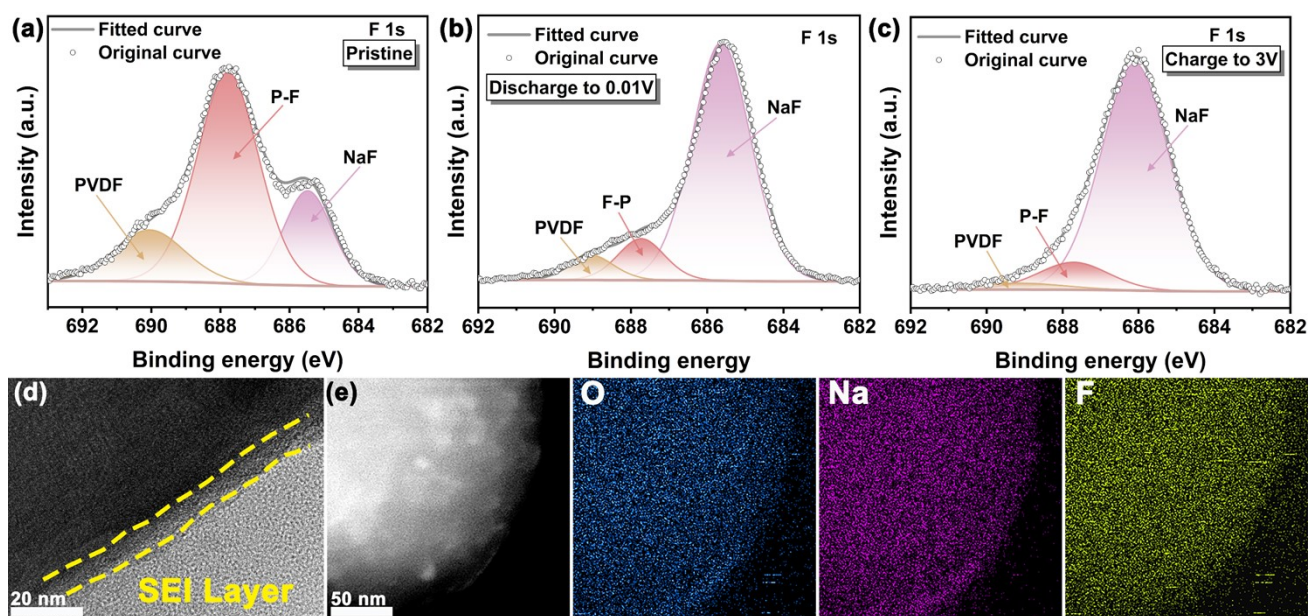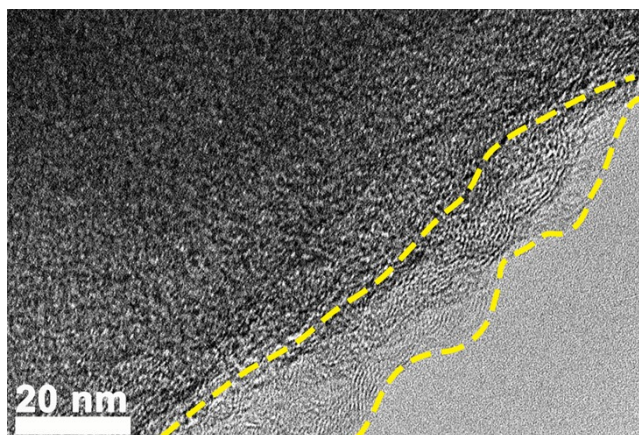**Fig. S19** EIS testing for CDRTF and CDRF

Fig. S20 F 1s energy spectra of CDRTF electrode sheet at different potentials during the first charging and discharging process (a) Initial state, (b) Discharging to 0.01 V, (c) Charging to 3 V after 2000 cycles (d) HRTEM, (e) EDS energy spectrum analysis.

Fig. S21 HRTEM images of CDRF

The ex-situ XPS spectra of F 1s are shown in Fig. S20a-c. In the initial state, a small amount of NaF appeared as the electrode was soaked by the electrolyte. When discharged to 0.01 V, the amount of NaF increased dramatically, indicating that an SEI membrane was formed during the cycling process. The SEI film was further stabilized during the subsequent charging process.

The SEI film has good electrical conductivity to Na^+ and is also an insulator for electrons, which was further stabilized and thin and uniform during the subsequent cycling process (Fig. S20d). The EDS energy spectrum shows a uniform distribution of O, F, and Na elements in CDRTF after 2000 charge-discharge cycling (Fig. S20e), which further illustrates the formation of the SEI film during the cycling process. HRTEM image of the SEI membrane of the CDRF sample, as shown in Fig. S21. When compared to the CDRTF sample, the SEI of the CDRF sample exhibits a thicker and inhomogeneous layer. So CDRTF sample has excellent compatibility with the electrolyte, which contributes to the performance enhancement.
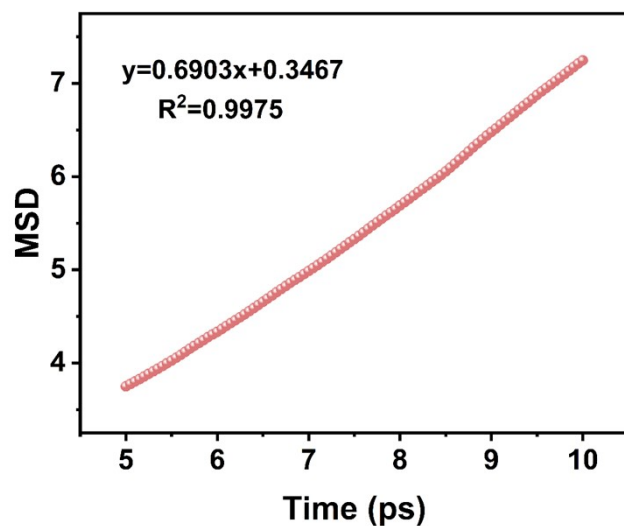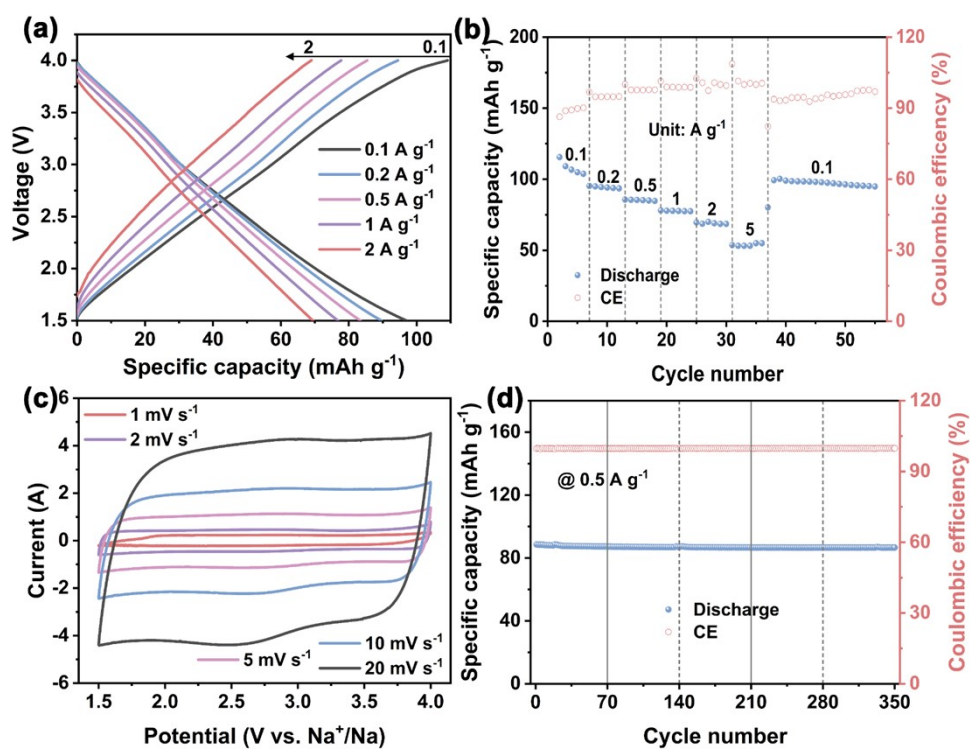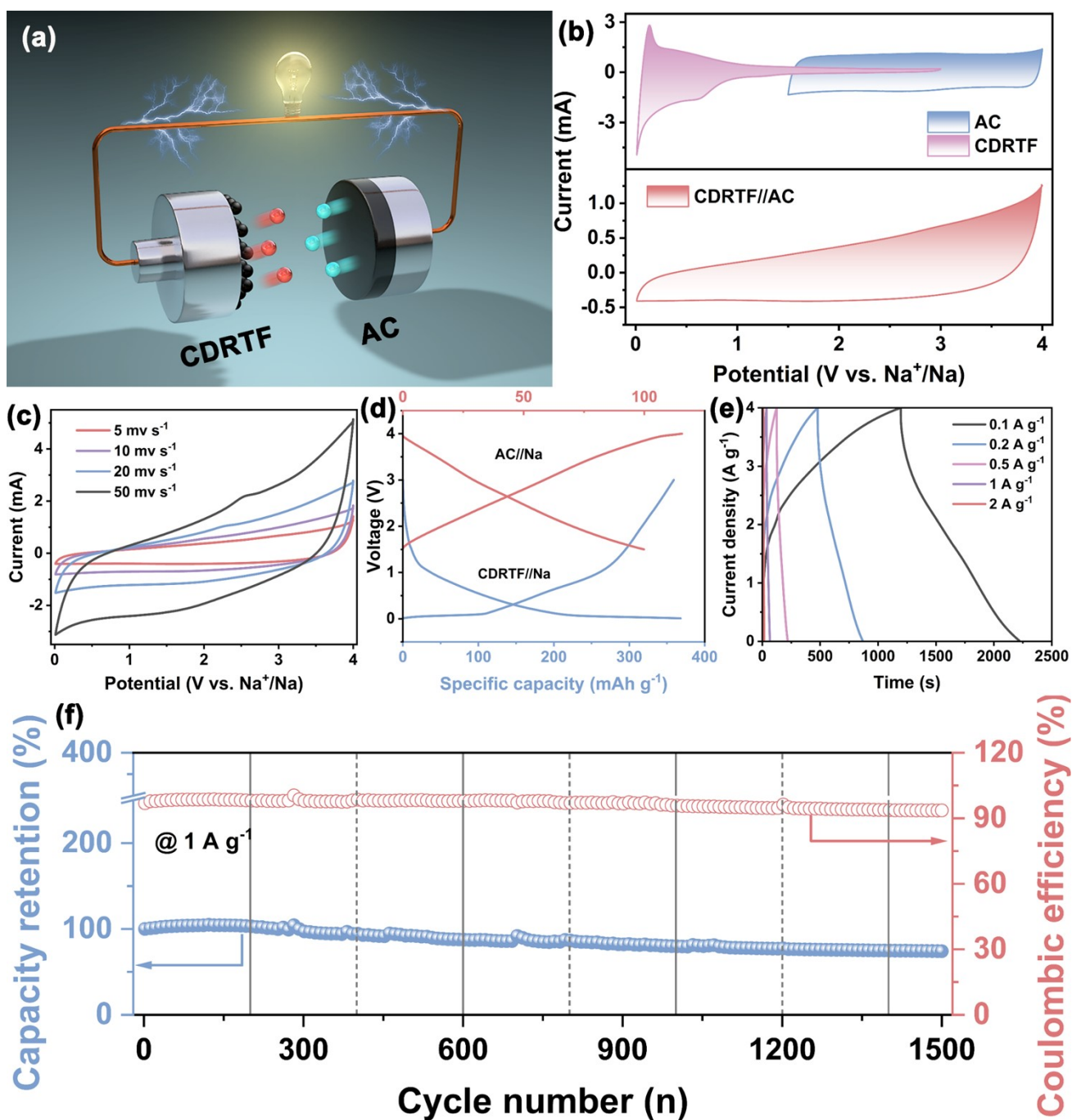
Fig. S22 MSD versus time plots.

Fig. S23 Electrochemical characterization of AC cathode associated with half-cell at 1.5-4 V. (a) GCD plots at different current densities, (b) rate performance, (c) CV plots at different scan rates, (d) long cycles.

Fig. S24 (a) Schematic diagram of the assembled CDRTF//AC SIC, (b) CV plots of CDRTF anode, AC cathode, and CDRTF//AC SIC at 5 mV s^{-1}, (c) CV curves of CDRTF//AC SIC at different current densities, (d) GCD curves of the CDRTF anode and AC cathode at 0.05 A g^{-1}, (e) GCD curves of CDRTF//AC SIC at different current densities, (f) long cycle of CDRTF//AC SIC at 1 A g^{-1}.

As shown in Fig. S22a, the CDRTF//AC SICs was assembled using by the pre-sodiumized CDRTF anode and AC cathode, and the consistency matching of the CDRTF anode with the AC

cathode was carried out at 5 mV s^{-1} (Fig. S22b). The CV tests of the CDRTF//AC SIC was carried out in the voltage interval from 0.01-4.0 V (Fig. S22c). Their CV curves exhibited a rectangle-like shape at different scan rates, and without severe distortion and electrolyte decomposition even at high scan rate of 50 mV s^{-1} (Fig. S22d), which indicates the reasonable matching of cathode and anode. Fig. S22e shows the GCD curves of the CDRTF//AC SIC at different current densities. Their GCD curves maintain the isosceles triangular shape and are also able to maintain their shapes at high current densities, indicating good electrochemical reversibility. The CDRTF//AC SIC was subjected to a long cycling test at 1 A g^{-1} (Fig. S22f), and the capacity retention reached 75.16 % after 1500 charge/discharge cycles. The acceptable stability was attributed to the increase in the resistance of the surface SEI film with the increase in the number of cycles as well as the depletion of the electrolyte, leading to the capacity degradation.
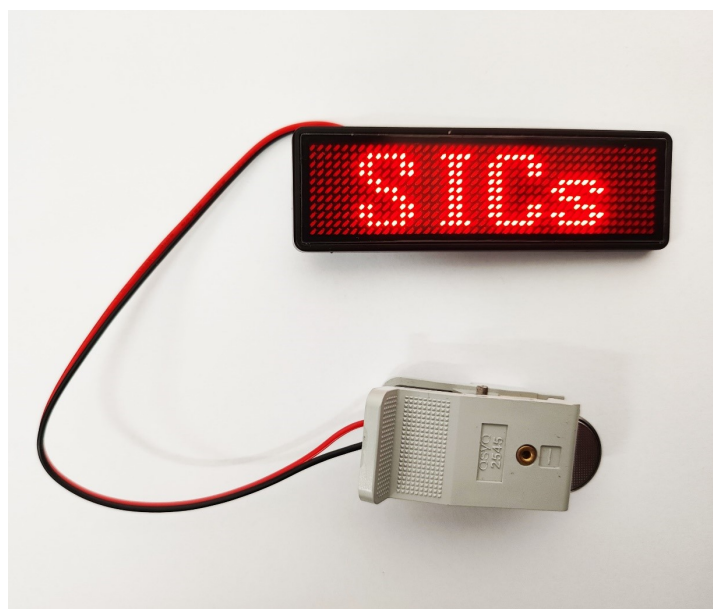
Fig. S25 LEDs driven by CDRTF//AC SICs

[1] L. He, W. Sun, K. Sun, Y. Mao, T. Deng, L. Fang, Z. Wang, S. Chen, *J. Power Sources*, 2022, **526**, 231019.

[2] H. Zhang, Z. Chen, Z. Sun, M. Cai, W. Liu, W. Ye, H. Gao, J. Han, Y. Cheng, Q. Zhang, M. Wang, *Adv. Funct. Mater.*, 2023, **33**, 2300769.

[3] Z. Zheng, S. Hu, W. Yin, J. Peng, R. Wang, J. Jin, B. He, Y. Gong, H. Wang, H. Fan, *Adv. Energy Mater.*, 2024, **14**, 2303064.

[4] G. Cheng, W. Zhang, W. Wang, H. Wang, Y. Wang, J. Shi, J. Chen, S. Liu, M. Huang, D. Mitlin, *Carbon Energy*, 2022, **4**, 986-1001.

[5] Q. He, H. Chen, X. Chen, J. Zheng, L. Que, F. Yu, J. Zhao, Y. Xie, M. Huang, C. Lu, J. Meng, X. Zhang, *Adv. Funct. Mater.*, 2024, **34**, 2310226.

[6] J. Xia, D. Yan, L. Guo, X. Dong, W. Li, A. Lu, *Adv. Mater.*, 2020, **32**, 2000447.

[7] Q. Meng, B. Chen, W. Jian, X. Zhang, S. Sun, T. Wang, W. Zhang, *J. Power Sources*, 2023, **581**, 233475.

[8] M. Song, Z. Yi, R. Xu, J. Chen, J. Cheng, Z. Wang, Q. Liu, Q. Guo, L. Xie, C. Chen, *Energy Storage Mater.*, 2022, **51**, 620-629.

[9] J. Yang, X. Wang, W. Dai, X. Lian, X. Cui, W. Zhang, K. Zhang, M. Lin, R. Zou, K. Loh, Q. Yang, W. Chen, *Nano-Micro Lett.*, 2021, **13**, 98.

[10] Z. Song, M. Di, S. Chen, Y. Bai, *Chem. Eng. J.*, 2023, **470**, 144237.

[11] Z. Tang, R. Zhang, H. Wang, S. Zhou, Z. Pan, Y. Huang, D. Sun, Y. Tang, X. Ji, K. Amine M. Shao, *Nat. Commun.*, 2023, **14**, 6024.

[12] Y. Zhao, Z. Hu, C. Fan, P. Gao, R. Zhang, Z. Liu, J. Liu, J. Liu, *Small*, 2023, **19**, 2303296.

[13] C. Qiu, A. Li, D. Qiu, Y. Wu, Z. Jiang, J. Zhang, J. Xiao, R. Yuan, Z. Jiang, X. Liu, X. Chen, H.

Song, *ACS Nano*, 2024, **18**, 11941–11954.

[14] Y. Wang, Z. Yi, L. Xie, Y. Mao, W. Ji, Z. Liu, X. Wei, F. Su, C. Chen, *Adv. Mater.*, 2024, 2401249.